Enhancement of photon blockade via topological edge states

Jun Li,[1,2,*] C.-M. Hu,[2,†] and Yaping Yang[1,‡]

[1] *MOE Key Laboratory of Advanced Micro-Structured Materials, School of Physics Science and Engineering, Tongji University, Shanghai 200092, China*

[2] *Department of Physics and Astronomy, University of Manitoba, Winnipeg R3T 2N2, Canada*

(Received 27 November 2023; revised 30 January 2024; accepted 15 March 2024; published 27 March 2024)

Quantum technologies, holding the promise of exponentially superior performance in comparison to their classical counterparts for certain tasks, have consistently encountered challenges, including instability in quantum light sources, quantum decoherence, and vulnerability to losses that topological photonics happens to adeptly address. Here, we theoretically put forth a quantum Su-Schrieffer-Heeger-type chain designed to greatly enhance single-photon blockade (single PB) effect with topological protection. By designing the deliberate coupling strengths, the quantum level lattices take the form of a one-dimensional array with a topological edge state in single-excitation space and a two-dimensional square breathing lattice with topological corner states in two-excitation space, resulting in enhanced single-photon excitation and the suppression of two-photon transitions. Therefore, the second-order correlation function is diminished by up to 2 orders of magnitude at the cavity resonance frequency, accompanied by stronger brightness. Furthermore, the PB effect is robust to local perturbations in cavity-qubit coupling and qubit frequency, benefitting from topological protection.

DOI: 10.1103/PhysRevApplied.21.034058

I. INTRODUCTION

Since 2005, topological photonics [1,2], inspired by topological band theory initially discovered in solid-state electron systems, was first proposed in photonic crystals [3,4] and so far has been extensively investigated across various platforms, including waveguides [5], cavities [6,7], metamaterials [8], optomechanics [9], ultracold atoms [10], rf circuits [11,12], and Fock-state lattices [13,14]. Further, optical systems also offer unprecedented opportunities to promote the exploration of alternative topological physics and actualize exceptional topological phenomena owing to their remarkable flexibility, diversity, and unique effects, e.g., non-Hermitian topology [15], Floquet topological insulators [5,16], topological photonics in synthetic dimensions [17], and nonlinear topological photonics [18].

In the context of bulk-edge correspondence, topological edge states (TESs) in open boundary conditions are naturally robust against local defects and disorders, attributable to the globally defined topological invariants. This characteristic enables a diverse array of devices and applications for addressing pervasive environmental effects by employing topological photonics, such as wireless power transfer [19,20], optical beam splitter [21], sensor [22], and nonreciprocity [16] in one dimension based on the Su-Schrieffer-Heeger (SSH) model [23] and topological laser [24,25], slow light [26,27], channel-drop filter [28], and four-wave mixing [29] in two dimensions. In particular, quantum light, acting as carriers of quantum information and quantum computing, still encounter challenges related to energy dissipation and decoherence stemming from external environment and system disorder. The emergence of topological photonic states represents a captivating research avenue to tackle this challenge [30,31]. In recent years, some pioneering experiments have showcased the robust generation and routing of quantum states in topological photonic integrated platforms [32–35].

Photon blockade (PB) effect serves as a significant technique for generating quantum light sources by effectively suppressing certain photon-number excitations in nonlinear systems. There are two physical mechanisms on which PB relies, i.e., the conventional photon blockade (CPB) [36,37] and the unconventional photon blockade (UPB) [38–40]. Specifically, the CPB is achieved through eigenenergy-level anharmonicity (ELA) originating from strong nonlinearity. The latter is induced by quantum destructive interference (QDI) between two or more individual quantum transition pathways. Generally, in comparison to CPB, the UPB exhibits a higher degree of antibunching, but the brightness is relatively poor. Recently, photon antibunching and corresponding mean photon number are both substantially improved by combining

*Corresponding authors: jli_phys@tongji.edu.cn
†hu@physics.umanitoba.ca
‡yang_yaping@tongji.edu.cn

the conventional ELA-induced and QDI-induced single-photon blockade (single PB) in a two-qubit driven cavity quantum electrodynamics (QED) system with dipole-dipole interaction [41]. Interestingly, the UPB is proposed to be enhanced in a chain of coupled resonators with exponentially suppressed nonlinearity requirement [42].

In this work, we propose a one-dimensional (1D) topological multiqubit-one-cavity chain, exhibiting notable advantages across various aspects compared to the Jaynes-Cummings (JC) model (a single-qubit-cavity system) under identical conditions [36]. They are (i) a reduction in the second-order correlation function by up to 2 orders of magnitude, signifying a higher probability of detecting a single photon; (ii) a larger mean photon number, advantageous for long-distance transmission and detection; (iii) operation at the cavity frequency independent of the cavity-qubit coupling strength; (iv) robustness against local perturbations in cavity-qubit coupling and qubit frequency, meeting the urgent requirements of quantum technology. Specifically, the quantum topological array comprises a linear optical cavity and a trivial dimer qubit lattice, established through the weaker coupling between the cavity and the boundary qubit. The quantum level lattice (QLL) in single-excitation space forms as an SSH chain with odd sites and possesses a zero-energy TES localized at the end of the single-photon excited state, thereby enabling a stronger intensity of single-photon excitation. Meanwhile, in two-excitation space, the zero-energy dressed state is localized at the corner of two-qubit excited states with the absence of a two-photon excited-state distribution. Furthermore, the dressed states near zero energy in the second manifold are the bulk states that hold quite weak distribution of the two-photon excited state. So that the single PB effect is significantly enhanced by the distinct TES distributions in the two manifolds. Moreover, the single PB effect in the quantum topological lattices also demonstrates robustness against the local disturbances in the cavity-qubit coupling strength and the qubit frequency.

II. MODEL AND QUANTUM LEVEL LATTICES

As shown in Fig. 1(a), we consider a 1D quantum topological array composed of a single-mode bosonic cavity and N_a ($N_a = 2N$, N is the number of unit cells) identical two-level systems (e.g., two-level qubits) arranged in a dimer chain (or SSH lattice) by coupling to their nearest neighbors with alternative hopping amplitudes J_1 and J_2. The optical cavity is coupled to one of the outermost qubit with the strength g and coherently driven by a monochromatic pump field with the Rabi frequency η and angular frequency ω_d. Here, all the coupling strengths are much smaller than the transition frequency of qubits ω_a and the resonant frequency of cavity ω_c. In rotating-wave approximation, the Hamiltonian of the driven multiqubit-cavity system is $H = H_a + H_c + H_i + H_d$, where (setting $\hbar = 1$)

$$\begin{aligned} H_a &= \Delta_a \sum_{i=1}^{N_a} \sigma_+^i \sigma_-^i + J_1 \sum_{i=1}^{N_a/2} \left(\sigma_+^i \sigma_-^{i+1} + \text{H.c.}\right) \\ &\quad + J_2 \sum_{i=1}^{N_a/2-1} \left(\sigma_+^{i+1} \sigma_-^{i+2} + \text{H.c.}\right), \\ H_c &= \Delta_c a^\dagger a, \quad H_i = g\left(a^\dagger \sigma_-^1 + \text{H.c.}\right), \\ H_d &= \eta\left(a^\dagger + a\right), \end{aligned} \tag{1}$$

where $\Delta_a = \omega_a - \omega_d$ is the qubit detuning with respect to the driving frequency and $\Delta_c = \omega_c - \omega_d$ is the cavity-driving detuning. Here, we focus on the simplest scenario where the frequency of the cavity and the qubits are identical ($\omega_a = \omega_c = \omega_0$), i.e., $\Delta_a = \Delta_c = \Delta$. $\sigma_+^i = |e\rangle\langle g|_i$ ($\sigma_-^i = |g\rangle\langle e|_i$) is the raising (lowering) operator of the ith two-level system and $a^\dagger$ (a) is the creation (annihilation) operation of the intracavity optical field.

In single-excitation space, the QLL of the system takes the form of a 1D lattice with an odd number of quantum state sites ($N_a + 1$) and is described by the Hamiltonian

$$H_I = \begin{pmatrix} 0 & g & 0 & 0 & \cdots \\ g & 0 & J_1 & 0 & \ddots \\ 0 & J_1 & 0 & J_2 & \ddots \\ 0 & 0 & J_2 & 0 & \ddots \\ \vdots & \ddots & \ddots & \ddots & \ddots \end{pmatrix}_{(N_a+1)\times(N_a+1)}, \tag{2}$$

which are identical to its classical lattice counterpart [see an example for $N_a = 4$ shown in Fig. 1(b)]. The lattice is expanded to two dimensions and comprises $N_a(N_a + 1)/2 + 1$ sites in two-excitation space for $N_a \geqslant 4$. The quantum states form a square lattice with triangle boundaries, constituting a two-order topological structure as illustrated in Fig. 1(c). In particular, due to the inherent nature of the annihilation operator $a|n\rangle = \sqrt{n}|n-1\rangle$, the coupling strength between the two-photon state $|g^{N_a}, 2\rangle$ and its nearest-neighbor state $|g^{N_a-1}e, 1\rangle$ is $\sqrt{2}g$. Additionally, the QLL in three-excitation space is represented as a three-dimensional cubic lattice with a triangular pyramid as the outline.

In this study, we consider the condition where $g < J_1$ and $J_2 < J_1$ to ensure that the QLL in single-excited space forms as a breathing SSH chain and the single-photon state $|g^{N_a}, 1\rangle$ is the sole weaker coupling termination in single-excitation lattice. Therefore, it can be inferred that there is an exactly zero-energy state exponentially localized to the end with one-photon state. Furthermore, we add the constraint $J_1 \leqslant \sqrt{2}g$ in order to prevent the two-photon state $|g^{N_a}, 2\rangle$ from being a relatively weaker coupling corner in two-excitation lattice for $N_a \geqslant 4$. Instead, as shown

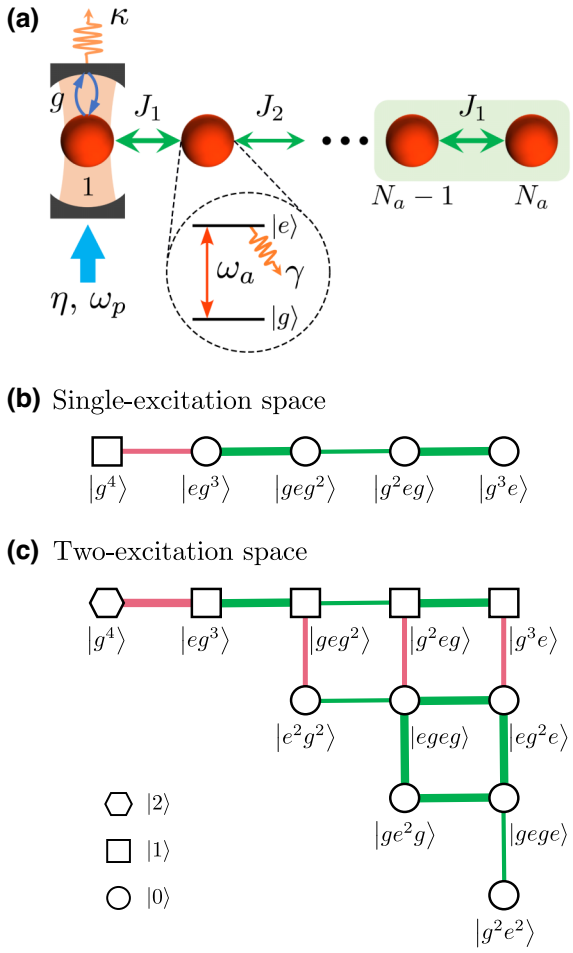

FIG. 1. (a) Schematic of considered multiqubit-cavity topological chain characterized by an optical cavity (resonant frequency ω_c) coupled to the first site of a dimer two-level lattice with the strength g. The dimer lattice, whose unit cells are marked by a green box, consists of N_a identical two-level qubits with the transition frequency ω_a between ground state $|g\rangle$ and excited state $|e\rangle$. The intracell and intercell hopping amplitudes of the lattice are J_1 and J_2, respectively. The cavity (qubit) decay rate is κ (γ). QLL in (b) single-excitation space and (c) two-excitation space for $N_a = 4$. The states labeling the lattice sites are the corresponding positional distributions of the qubit states with the power of the exponent representing the number of repetitions of adjacent qubit states. For clarity, we use circles, squares, and a hexagon in (b),(c) to denote the cavity photon states $|0\rangle$, $|1\rangle$, and $|2\rangle$, respectively. The widths of the lines connecting neighboring states represent the coupling strengths between them.

in Fig. 1(c), the two-qubit excited state $|g^{N_a-2}e^2, 0\rangle$ always serves as a weakly coupled corner. Thus, the topological zero-energy state in two-excitation space is predominantly distributed at the two-qubit excited state $|g^{N_a-2}e^2, 0\rangle$ rather than the two-photon state $|g^{N_a}, 2\rangle$. By combining the aforementioned two conditions, it is expected that the single PB effect will occur at the resonance frequency of the cavity.

Based on the Born-Markov approximation, the dynamic density matrix ρ of the entire system with dissipation is governed by the master equation

$$\frac{\partial \rho}{\partial t} = -i[H, \rho] + \frac{\kappa}{2}\mathcal{L}_\rho[a] + \frac{\gamma}{2}\sum_{i=1}^{N_a}\mathcal{L}_\rho[\sigma_-^i], \tag{3}$$

where $\mathcal{L}_\rho[a] = 2a\rho a^\dagger - a^\dagger a\rho - \rho a^\dagger a$ indicates the cavity leakage at rate κ and $\mathcal{L}_\rho[\sigma_-^i] = 2\sigma_-^i\rho\sigma_+^i - \sigma_+^i\sigma_-^i\rho - \rho\sigma_+^i\sigma_-^i$ denotes the spontaneous decay of the excited state of the ith qubit at rate γ. Here, we consider the topological lattices function as conventional photon blockade, achieved through ELA in the strong-coupling regime, where the losses of the system are much smaller than the coupling strength.

III. ENHANCEMENT OF PHOTON BLOCKADE

In the absence of the driven field and system dissipation, we can numerically obtain the eigenvalues $E_{\pm i}^n$ and their corresponding eigenstates $\Phi_{\pm i}^n$, where the superscript $n \in [0, 1, 2, \ldots]$ indicates the order of the manifold and the subscript $\pm i$ denotes ith symmetric eigenstates with reference to zero energy in each space. By setting the normalized hopping amplitudes $J_1/g = \sqrt{2}$ and $J_2/g = 0.2$, we plot the corresponding eigenvalue structures of our topological array for the simpler cases of $N_a = 2$ in Fig. 2(b) and $N_a = 4$ in Fig. 2(c), respectively. As expected, in the first manifold, there always exists an exact zero-energy dressed state $\Phi_0^1 = C_1|g^{N_a}, 1\rangle + C_2|eg^{N_a-1}, 0\rangle + \cdots + C_{N_a+1}|g^{N_a-1}e, 0\rangle$ that is exponentially localized at the single-photon state $|g^{N_a}, 1\rangle$ [as exemplified in Fig. 2(d) for $N_a = 4$], with the normalized amplitudes $C_1 > 0.8$ and $C_{2x} = 0$ ($x \in [1, \ldots, N]$) as N_a varies. In the second manifold, the zero-energy dressed level is absent for the simplest case of $N_a = 2$ as shown in Fig. 2(b). For $N_a \geqslant 4$, there are $Na/2 - 1$ zero-energy states primarily distributed among the two-qubit excited states, without any distribution at the two-photon excited state [as shown in Fig. 2(f) for $N_a = 4$]. Moreover, for comparison, we include the dressed-state diagram of coupled single-qubit-cavity system (JC model) in Fig. 2(a), where there is no zero-energy state in any manifold.

The single PB effect behaviors are quantified by the equal-time second-order correlation function $g^{(2)}(0)$, which can be calculated by

$$g^{(2)}(0) = \frac{\langle a^{\dagger 2}a^2\rangle}{\langle a^\dagger a\rangle^2} = \frac{Tr\left(a^{\dagger 2}a^2\rho\right)}{\left[Tr\left(a^\dagger a\right)\right]^2}, \tag{4}$$

where the density matrix ρ is obtained by numerically solving Eq. (2) based on the QuTiP [43] and the QuantumOptics.jl toolbox [44].

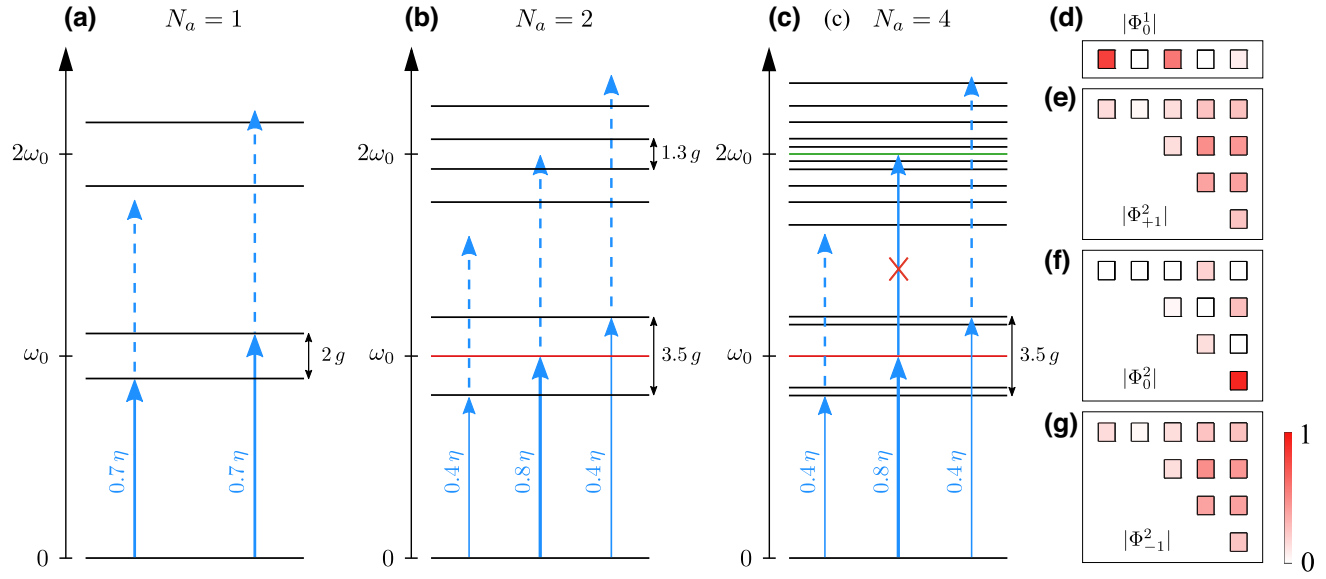

FIG. 2. The dressed-state structures and the main transition pathways of the considered qubit-cavity coupled system with the number of qubits (a) $N_a = 1$ (JC model), (b) $N_a = 2$, and (c) $N_a = 4$. The levels labeled by red in (b),(c) are the topological edge modes in single-excitation space while the green level in (c) is the topological corner state in two-excitation space. The single blue arrows in (a)–(c) denote the excitation pathways of photon blockade (PB) where the dashed arrows indicate the ELA. The wave-function distributions of (d) the topological zero-energy states $|\Phi_0^1$ in single-excitation space, (f) the zero-energy corner-localized state Φ_0^2, and (e),(g) the bulk states $\Phi_{\pm 1}^2$ in two-excitation space for $N_a = 4$. The layout of sites in (d),(e)–(g) is accordance with that shown in Figs. 1(b) and 1(c), respectively. Here, we take the parameter relations $J_1 = \sqrt{2}g$ and $J_2 = 0.2g$.

With the same normalized system parameters $g/\gamma = 10$ and $\kappa/\gamma = 0.5$, Figs. 3(a)–(c) show the logarithmic plots of equal-time second-order correlation function $\log_{10}[g^{(2)}(0)]$ as a function of the detuning Δ/γ and driven strength η/γ for different numbers of qubits $N_a = 1$, 2, and 4, respectively. The corresponding mean photon

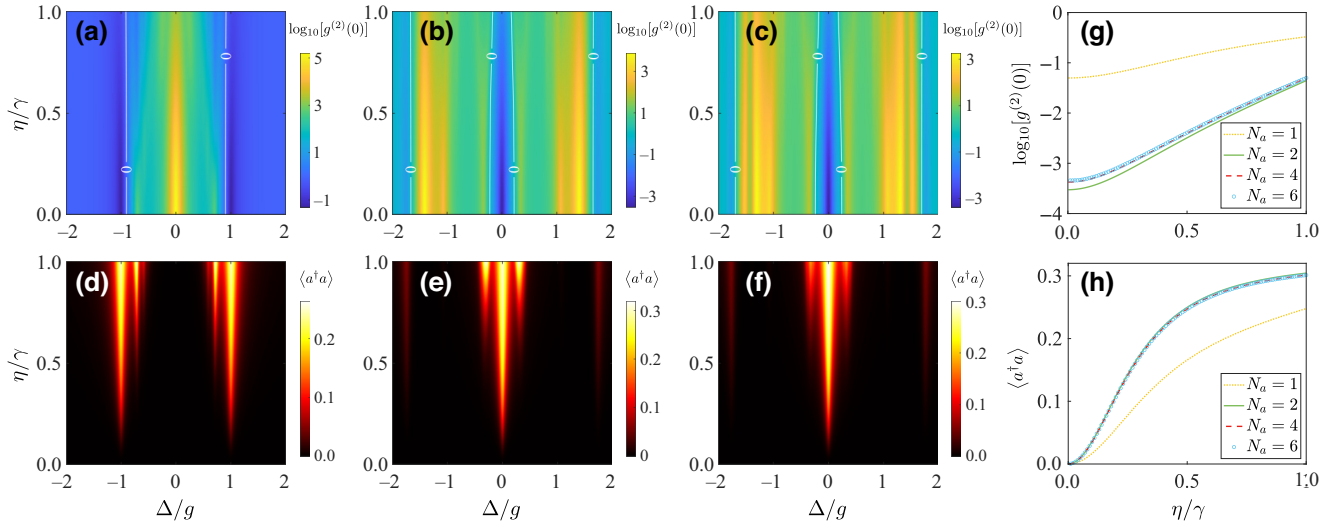

FIG. 3. (a)–(c) The equal-time second-order correlation function $\log_{10}[g^{(2)}(0)]$ and (d)–(f) the corresponding mean photon number $\langle a^\dagger a\rangle$ mapping on the plane of normalized detuning Δ/g and driven strength η/γ for (a),(d) $N_a = 1$, (b),(e) $N_a = 2$, and (c),(f) $N_a = 4$, respectively. The white curves in (a)–(c) denote the contours of $g^{(2)}(0) = 1$ for Poissonian statistics. (g) The optimal second-order correlation function and (h) the corresponding mean photon number versus the normalized pump field Rabi frequency η/γ for different N_a. The optimal conditions are $\Delta/g = \pm 1$ for $N_a = 1$ and $\Delta = 0$ for $N_a \geqslant 2$. Here, the system parameters are given by $g = 10\gamma$ and $\kappa = 0.5\gamma$. The other parameters are the same as those used in Fig. 2.

number $\langle a^\dagger a\rangle$ is displayed in Figs. 3(d)–3(f). In the single-qubit case, single PB occurs around the detuning $\Delta = \pm g$ due to the single-photon resonance with nonresonant two-photon excitations as depicted in Fig. 2(a) [36,37]. For our multiqubit-cavity topological chain, as clearly shown in Figs. 3(b) and 3(c), there are three regimes of single PB ($g^{(2)}(0) < 1$) with the detuning $\Delta = 0$ and $\Delta \approx \pm 1.8g$ on the plane, which correspond to the single-photon excitation process from the ground state $|g^{N_a}, 0\rangle$ to the TES Φ_0^1 and the bulk states $\Phi_{\pm N_a/2}^1$ of QLL in single-excitation space, respectively. Particularly, the resonance-driven scenario shows a significantly smaller second-order correlation function, indicating strong single-photon antibunching. Meanwhile, higher mean photon-number peak concomitantly appears due to the stronger single-photon excitation probability. Moreover, the frequency range for achieving single PB around $\Delta = 0$ slightly expands as the number of qubits N_a increases.

For the sake of comparison, we present the optimal second-order correlation function $\log_{10}[g^{(2)}(0)]$ in the frequency domain against the normalized pump strength η/γ for different numbers of qubits in Fig. 3(g), along with the corresponding mean photon number $\langle a^\dagger a\rangle$ in Fig. 3(h). Obviously, in comparison to the JC model ($N_a = 1$), the multiqubit-cavity lattices ($N_a \geqslant 2$) exhibit up to 2 orders of magnitude smaller $g^{(2)}(0)$, accompanied by larger mean photon number. For the two-qubit case, the enhancement of single PB arises from the greater two-photon excitation anharmonicity and the lower two-photon intensity of dressed states in the second manifold in contrast to the JC model. With an increasing number of qubits ($N_a \geqslant 4$), as depicted in Fig. 2(c), the number of dressed levels in the second manifold increases quadratically, resulting in smaller anharmonicity and the emergence of zero-energy dressed states Φ_0^2. However, in the resonance-driven case, there is only a slight variation in the second-order correlation function and the mean photon number. On the one hand, the resonant transition $\Phi_0^1 \to \Phi_0^2$ is strictly forbidden due to the lack of overlap between the wave-function distributions of the zero-energy states in the two manifolds on the same qubit states, as shown in Figs. 2(d) and 2(f). On the other hand, the dressed states with near-zero energy in the second manifold correspond to bulk states characterized by a weak intensity of two-photon state $|g^{N_a}, 2\rangle$ [see Figs. 2(e) and 2(g)]. Further, the intensity decreases as the number of qubits N_a increases, leading to the expansion of single PB region around $\Delta = 0$. In addition, the reduction of system losses, especially in the optical cavity, will result in a decrease in the second-order correlation function and an increase in the mean photon number due to reduced overlap between the anharmonic energy levels.

The enhancement of single PB can be further confirmed by comparing the photon-number distribution of the cavity field $P(n)$ with the Poisson distribution $\mathcal{P}(n) = \langle a^\dagger a\rangle^n e^{-\langle a^\dagger a\rangle}/n!$. In Fig. 4, we show the relative deviations of photon-number distribution with respect to the Poisson distribution with the same mean photon number, i.e., $[P(n) - \mathcal{P}(n)]/\mathcal{P}(n)$. In comparison to the JC model ($N_a = 1$) with the identical conditions, it is evident that $P(1)$ in the multiqubit-cavity system ($N_a \geqslant 2$) is more strongly enhanced while $P(n > 1)$ are significantly suppressed, indicating the higher probability for detecting a single photon. Moreover, the probability distribution $P(1)$ is also greatly enhanced as the driven strength increases.

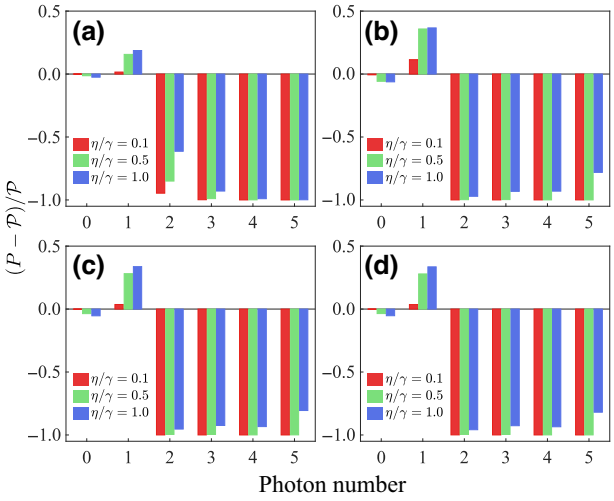

FIG. 4. The deviations of the photon distribution to the standard Poisson distribution with the same mean photon number for (a) $N_a = 1$, (b) $N_a = 2$, (c) $N_a = 4$, and (d) $N_a = 6$, respectively. The cavity-driving detuning is $\Delta = \pm g$ for $N_a = 1$ and $\Delta = 0$ for $N_a \geqslant 2$. The other system parameters are the same as those used in Fig. 3.

IV. ROBUSTNESS OF PHOTON BLOCKADE

The PB effect of our quantum topological array effectively incorporates and demonstrates the inherent topological protection property of the SSH chain that are insensitive to local perturbations. Here, we examine the robustness of the single PB phenomenon in the presence of perturbations by considering specific examples of disturbances in the cavity-qubit coupling strength δ_g and the transition frequency of the first qubit $\delta_{\omega 1}$. In Fig. 5, by considering the cavity-qubit coupling strength $g' = g + \delta_g$, we present the evolution of the second-order correlation function $\log_{10}[g^{(2)}(0)]$ and the corresponding cavity mean photon number $\langle a^\dagger a\rangle$ versus the fluctuation strength of cavity-qubit coupling δ_g with $\eta/\gamma = 0.5$ for different N_a. Predictably, in the JC model, the optimal operating frequency for achieving single PB experiences a linear shift in response to the fluctuation strength of the cavity-qubit coupling due to the linear coupling-dependent dressed levels

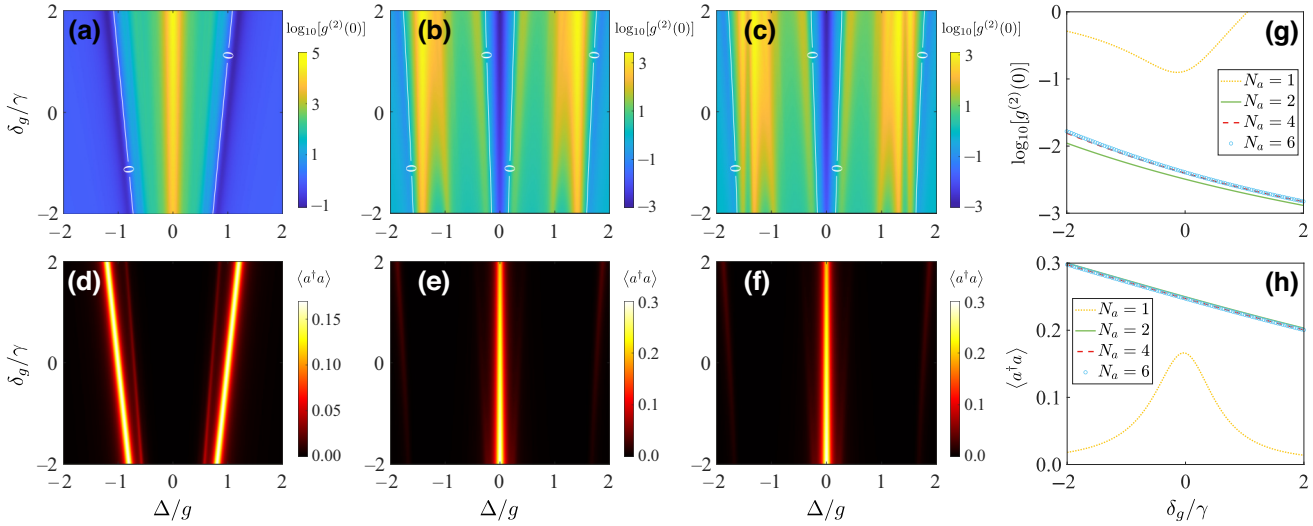

FIG. 5. The influences of fluctuation strength of cavity-qubit coupling δ_g. (a)–(c) Steady-state second-order correlation function $\log_{10}[g^{(2)}(0)]$ and (d)–(f) cavity mean photon number $\langle a^\dagger a\rangle$ plotted as a function of the normalized detuning Δ/g and fluctuation strength δ_g/γ with the driven strength $\eta/\gamma = 0.5$ for (a),(d) $N_a = 1$, (b),(e) $N_a = 2$, and (c),(f) $N_a = 4$, respectively. (g) The second-order correlations and (h) the corresponding mean photon number in relation to the normalized fluctuation strength δ_g/γ with the detuning $\Delta = \pm g$ for $N_a = 1$ and $\Delta = 0$ for $N_a \geqslant 2$. All other parameters remain the same as those utilized in Fig. 3.

in the first manifold. In contrast, in the case of multiqubit-cavity arrays ($N_a \geqslant 2$), the optimal operating frequency, which yields the smallest second-order correlation function $g^{(2)}(0)$ and the largest mean photon number $\langle a^\dagger a\rangle$, consistently remains at the resonance frequency of the cavity regardless of variations in the cavity-qubit coupling strength. For the resonance-driven condition, $g^{(2)}(0)$ and the mean photon number $\langle a^\dagger a\rangle$ decrease (increase) with increasing (decreasing) cavity-qubit coupling strength, owing to the heightened (depressed) two-photon excitation anharmonicity and single-photon excitation probability, respectively. As clearly shown in Figs. 5(g) and 5(h), compared with the single-qubit cavity system, the second-order correlation function and mean photon number of the quantum topological arrays are more robust to the cavity-qubit coupling fluctuation at a fixed operating frequency.

For the diagonal perturbation, we show the developments of correlation function and corresponding cavity

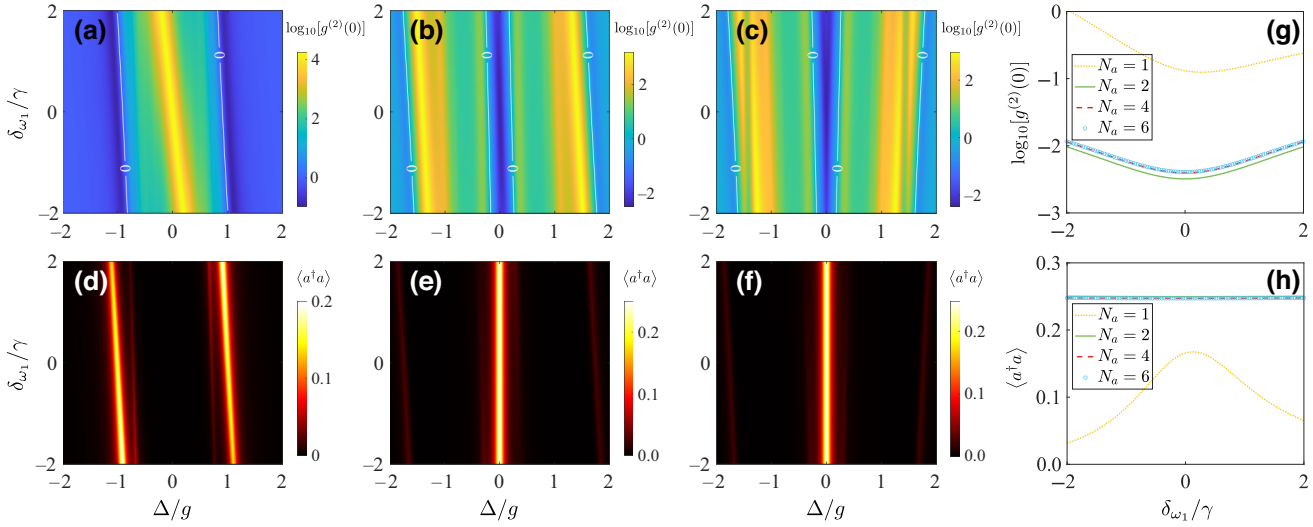

FIG. 6. The effects of the first qubit's transition frequency shift $\delta_{\omega 1}$. Plots of (a)–(c) $\log_{10}[g^{(2)}(0)]$ and (d)–(f) $\langle a^\dagger a\rangle$ as a function of the normalized detuning Δ/g and frequency shift $\delta_{\omega 1}/\gamma$ with $\eta/\gamma = 0.5$ for (a),(d) $N_a = 1$, (b),(e) $N_a = 2$, and (c),(f) $N_a = 4$, respectively. Profiles of (g) the second-order correlation function and (h) the corresponding mean photon number at the cavity-driving detuning $\Delta = g$ for $N_a = 1$ and $\Delta = 0$ for $N_a \geqslant 2$. The other system parameters are the same as those employed in Fig. 3.

mean photon number with the normalized frequency shift of the qubit coupled to cavity $\delta_{\omega 1}/\gamma$ as shown in Fig. 6. For single-qubit condition, the optimal pump frequency to achieve PB with a brighter mean photon number is directly related to the qubit frequency, which is not conducive to manipulation in practical applications. Contrastingly, the multiqubit-cavity chain maintains an almost constant mean photon number at the cavity resonance frequency, given that the frequency and distribution of TES in the single-excitation space are hardly affected by the transition frequency of the qubit. Simultaneously, in the two-excitation space, the distribution density of the zero-energy state on the two-photon excited state is no longer entirely zero with a nonzero qubit frequency shift. This leads to a gradual increase in the second-order correlation function with the increasing qubit frequency shift for the resonance-driven condition. 6

V. DISCUSSION AND CONCLUSION

The proposed scheme holds the potential for implementation in various quantum systems, such as coupled atom-array-cavity QED [45,46], quantum dot array [47], and particularly in integrated superconducting quantum circuits [14,48–51]. Previous works have implemented a one-dimensional circuit QED lattice of 72 qubit-coupled microwave cavities with coherent driving [48] and demonstrated a coupled 24-qubit array [50]. Circuit QED also serves as a controllable platform with tunable strong coupling strengths achieved by manipulating the magnetic flux of the inductive coupler [14]. The quantum lattice with breathing coupling, requiring only a few coupled qubits (at least two), can be implemented more easily using the existing mature circuit QED lattice.

In summary, we have investigated an enhanced conventional photon blockade effect utilizing a 1D cascading coupled multiqubit-one-cavity array based on the SSH model. One-sided localized topological edge states of the QLL in single-excitation space empower the system to exhibit a stronger intensity of single-photon excitation at the resonance frequency while two-photon excitation is effectively suppressed due to the forbidden resonance excitation and diffusely distributed bulk states in two-excitation space. The quantum topological chain exhibits a robust single PB effect, achieving up to a 2 orders of magnitude improvement in the second-order correlation function yet enhancing the mean photon number simultaneously. Our work contributes a theoretical framework for the preparation of high-quality and high-brightness single-photon source with strong robustness.

ACKNOWLEDGMENTS

National Natural Science Foundation of China (Grant No. 12274326); National Key Research and Development Program of China (Grants No. 2021YFA1400600, No. 2021YFA1400602); (Grant No. 202106260079). C.-M. Hu acknowledges support from NSERC Discovery Grants and NSERC Discovery Accelerator Supplements.

[1] L. Lu, J. D. Joannopoulos, and M. Soljačić, Topological photonics, Nat. Photonics **8**, 821 (2014).
[2] T. Ozawa, H. M. Price, A. Amo, N. Goldman, M. Hafezi, L. Lu, M. C. Rechtsman, D. Schuster, J. Simon, O. Zilberberg, and I. Carusotto, Topological photonics, Rev. Mod. Phys. **91**, 015006 (2019).
[3] F. D. M. Haldane and S. Raghu, Possible realization of directional optical waveguides in photonic crystals with broken time-reversal symmetry, Phys. Rev. Lett. **100**, 013904 (2008).
[4] Z. Wang, Y. Chong, J. D. Joannopoulos, and M. Soljačić, Observation of unidirectional backscattering-immune topological electromagnetic states, Nature **461**, 772 (2009).
[5] M. C. Rechtsman, J. M. Zeuner, Y. Plotnik, Y. Lumer, D. Podolsky, F. Dreisow, S. Nolte, M. Segev, and A. Szameit, Photonic Floquet topological insulators, Nature **496**, 196 (2013).
[6] M. Hafezi, E. A. Demler, M. D. Lukin, and J. M. Taylor, Robust optical delay lines with topological protection, Nat. Phys. **7**, 907 (2011).
[7] K. Fang, Z. Yu, and S. Fan, Realizing effective magnetic field for photons by controlling the phase of dynamic modulation, Nat. Photonics **6**, 782 (2012).
[8] S. Ma, B. Yang, and S. Zhang, Topological photonics in metamaterials, Photonics Insights **1**, R02 (2022).
[9] M. Schmidt, S. Kessler, V. Peano, O. Painter, and F. Marquardt, Optomechanical creation of magnetic fields for photons on a lattice, Optica **2**, 635 (2015).
[10] N. R. Cooper, J. Dalibard, and I. B. Spielman, Topological bands for ultracold atoms, Rev. Mod. Phys. **91**, 015005 (2019).
[11] V. V. Albert, L. I. Glazman, and L. Jiang, Topological properties of linear circuit lattices, Phys. Rev. Lett. **114**, 173902 (2015).
[12] J. Ningyuan, C. Owens, A. Sommer, D. Schuster, and J. Simon, Time- and site-resolved dynamics in a topological circuit, Phys. Rev. X **5**, 021031 (2015).
[13] H. Cai and D.-W. Wang, Topological phases of quantized light, Natl. Sci. Rev. **8**, 00 (2020).
[14] J. Deng, H. Dong, C. Zhang, Y. Wu, J. Yuan, X. Zhu, F. Jin, H. Li, Z. Wang, H. Cai, C. Song, H. Wang, J. Q. You, and D.-W. Wang, Observing the quantum topology of light, Science **378**, 966 (2022).
[15] E. J. Bergholtz, J. C. Budich, and F. K. Kunst, Exceptional topology of non-hermitian systems, Rev. Mod. Phys. **93**, 015005 (2021).
[16] J. Li, B. Gao, C. Zhu, J. Xu, and Y. Yang, Nonreciprocal photonic composited Su–Schrieffer–Heeger chain, Appl. Phys. Lett. **119**, 141108 (2021).
[17] E. Lustig and M. Segev, Topological photonics in synthetic dimensions, Adv. Opt. Photonics **13**, 426 (2021).
[18] D. Smirnova, D. Leykam, Y. Chong, and Y. Kivshar, Nonlinear topological photonics, Appl. Phys. Rev. **7**, 021306 (2020).

[19] J. Song, F. Yang, Z. Guo, X. Wu, K. Zhu, J. Jiang, Y. Sun, Y. Li, H. Jiang, and H. Chen, Wireless power transfer via topological modes in dimer chains, Phys. Rev. Appl. **15**, 014009 (2021).
[20] L. Zhang, Y. Yang, Z. Jiang, Q. Chen, Q. Yan, Z. Wu, B. Zhang, J. Huangfu, and H. Chen, Demonstration of topological wireless power transfer, Sci. Bull. **66**, 974 (2021).
[21] W. Song, W. Sun, C. Chen, Q. Song, S. Xiao, S. Zhu, and T. Li, Robust and broadband optical coupling by topological waveguide arrays, Laser Photon. Rev. **14**, 1900193 (2020).
[22] Z. Guo, T. Zhang, J. Song, H. Jiang, and H. Chen, Sensitivity of topological edge states in a non-hermitian dimer chain, Photonics Res. **9**, 574 (2021).
[23] W. P. Su, J. R. Schrieffer, and A. J. Heeger, Solitons in polyacetylene, Phys. Rev. Lett. **42**, 1698 (1979).
[24] G. Harari, M. A. Bandres, Y. Lumer, M. C. Rechtsman, Y. D. Chong, M. Khajavikhan, D. N. Christodoulides, and M. Segev, Topological insulator laser: Theory, Science **359**, eaar4003 (2018).
[25] M. A. Bandres, S. Wittek, G. Harari, M. Parto, J. Ren, M. Segev, D. N. Christodoulides, and M. Khajavikhan, Topological insulator laser: Experiments, Science **359**, eaar4005 (2018).
[26] H. Yoshimi, T. Yamaguchi, Y. Ota, Y. Arakawa, and S. Iwamoto, Slow light waveguides in topological valley photonic crystals, Opt. Lett. **45**, 2648 (2020).
[27] G. Arregui, J. Gomis-Bresco, C. M. Sotomayor-Torres, and P. D. Garcia, Quantifying the robustness of topological slow light, Phys. Rev. Lett. **126**, 027403 (2021).
[28] J.-X. Fu, J. Lian, R.-J. Liu, L. Gan, and Z.-Y. Li, Unidirectional channel-drop filter by one-way gyromagnetic photonic crystal waveguides, Appl. Phys. Lett. **98**, 211104 (2011).
[29] J. W. You, Z. Lan, and N. C. Panoiu, Four-wave mixing of topological edge plasmons in graphene metasurfaces, Sci. Adv. **6**, eaaz3910 (2020).
[30] Q. Yan, X. Hu, Y. Fu, C. Lu, C. Fan, Q. Liu, X. Feng, Q. Sun, and Q. Gong, Quantum topological photonics, Adv. Opt. Mater. **9**, 2001739 (2021).
[31] A. Blanco-Redondo, Topological nanophotonics: Toward robust quantum circuits, Proc. IEEE **108**, 837 (2020).
[32] S. Barik, A. Karasahin, C. Flower, T. Cai, H. Miyake, W. DeGottardi, M. Hafezi, and E. Waks, A topological quantum optics interface, Science **359**, 666 (2018).
[33] A. Blanco-Redondo, B. Bell, D. Oren, B. J. Eggleton, and M. Segev, Topological protection of biphoton states, Science **362**, 568 (2018).
[34] S. Mittal, E. A. Goldschmidt, and M. Hafezi, A topological source of quantum light, Nature **561**, 502 (2018).
[35] M. Wang, C. Doyle, B. Bell, M. J. Collins, E. Magi, B. J. Eggleton, M. Segev, and A. Blanco-Redondo, Topologically protected entangled photonic states, Nanophotonics **8**, 1327 (2019).
[36] K. M. Birnbaum, A. Boca, R. Miller, A. D. Boozer, T. E. Northup, and H. J. Kimble, Photon blockade in an optical cavity with one trapped atom, Nature **436**, 87 (2005).
[37] C. Hamsen, K. N. Tolazzi, T. Wilk, and G. Rempe, Two-photon blockade in an atom-driven cavity QED system, Phys. Rev. Lett. **118**, 133604 (2017).
[38] T. C. H. Liew and V. Savona, Single photons from coupled quantum modes, Phys. Rev. Lett. **104**, 183601 (2010).
[39] H. Flayac and V. Savona, Unconventional photon blockade, Phys. Rev. A **96**, 053810 (2017).
[40] H. J. Snijders, J. A. Frey, J. Norman, H. Flayac, V. Savona, A. C. Gossard, J. E. Bowers, M. P. van Exter, D. Bouwmeester, and W. Löffler, Observation of the unconventional photon blockade, Phys. Rev. Lett. **121**, 043601 (2018).
[41] C. J. Zhu, K. Hou, Y. P. Yang, and L. Deng, Hybrid level anharmonicity and interference-induced photon blockade in a two-qubit cavity QED system with dipole–dipole interaction, Photonics Res. **9**, 1264 (2021).
[42] Y. Wang, W. Verstraelen, B. Zhang, T. C. H. Liew, and Y. D. Chong, Giant enhancement of unconventional photon blockade in a dimer chain, Phys. Rev. Lett. **127**, 240402 (2021).
[43] J. Johansson, P. Nation, and F. Nori, Qutip: An open-source python framework for the dynamics of open quantum systems, Comput. Phys. Commun. **183**, 1760 (2012).
[44] S. Krämer, D. Plankensteiner, L. Ostermann, and H. Ritsch, Quantumoptics.jl: A Julia framework for simulating open quantum systems, Comput. Phys. Commun. **227**, 109 (2018).
[45] A. Cidrim, T. S. do Espirito Santo, J. Schachenmayer, R. Kaiser, and R. Bachelard, Photon blockade with ground-state neutral atoms, Phys. Rev. Lett. **125**, 073601 (2020).
[46] L. A. Williamson, M. O. Borgh, and J. Ruostekoski, Superatom picture of collective nonclassical light emission and dipole blockade in atom arrays, Phys. Rev. Lett. **125**, 073602 (2020).
[47] F. R. Braakman, P. Barthelemy, C. Reichl, W. Wegscheider, and L. M. K. Vandersypen, Long-distance coherent coupling in a quantum dot array, Nat. Nanotechnol. **8**, 432 (2013).
[48] M. Fitzpatrick, N. M. Sundaresan, A. C. Y. Li, J. Koch, and A. A. Houck, Observation of a dissipative phase transition in a one-dimensional circuit QED lattice, Phys. Rev. X **7**, 011016 (2017).
[49] C. Jones, M. A. Fogarty, A. Morello, M. F. Gyure, A. S. Dzurak, and T. D. Ladd, Logical qubit in a linear array of semiconductor quantum dots, Phys. Rev. X **8**, 021058 (2018).
[50] Y. Ye., *et al.*, Propagation and localization of collective excitations on a 24-qubit superconducting processor, Phys. Rev. Lett. **123**, 050502 (2019).
[51] X. Mi, *et al.*, Noise-resilient edge modes on a chain of superconducting qubits, Science **378**, 785 (2022).